

# Attosecond time-scale multi-electron collisions in the Coulomb four-body problem: traces in classical probability densities

Agapi Emmanouilidou<sup>1,2</sup> and Jan Michael Rost<sup>1,3</sup>

<sup>1</sup> KITP, University of California Santa Barbara, Santa Barbara, CA 93106

<sup>2</sup> ITS, University of Oregon, Eugene, Oregon 97403-5203

<sup>3</sup>Max Planck Institute for the Physics of Complex Systems, 01187 Dresden, Germany

(Dated: September 3, 2018)

In the triple ionization of the Li ground state by single photon absorption the three electrons escape to the continuum mainly through two collision sequences with individual collisions separated by time intervals on the attosecond scale. We investigate the traces of these two collision sequences in the classical probability densities. We show that each collision sequence has characteristic phase space properties which distinguish it from the other. Classical probability densities are the closest analog to quantum mechanical densities allowing our results to be directly compared to quantum mechanical results.

PACS numbers: 32.80.Fb

## I. INTRODUCTION

The theoretical treatment of multiple ionization processes by single photon absorption is highly complex with no analytic solution. In the energy domain, the difficulty is that one has to account for the correlated motion of the electrons in the asymptotic form of the final continuum state. In the time domain, this difficulty can be avoided at the expense of propagating the fully coupled few-body Coulomb problem in time.

One can surmount the obstacles in the theoretical treatment of the triple photo-ionization from the ground state of Lithium, for a wide range of energies, by formulating the four-body break-up process quasiclassically [1]. This implies classical propagation of the Coulomb four-body problem using the classical trajectory Monte Carlo (CTMC) phase space method. CTMC has often been used to describe break-up processes induced by particle impact [2, 3, 4, 5] with implementations differing usually in the way the phase space distribution of the initial state is constructed. We use a Wigner transform of the initial quantum wave function for the initial state, and this is why we call our approach “quasi”-classical. Naturally, the electron-electron interaction is treated to all orders in the propagation, and any difficulties with electron correlation in the final state are absent, since the method is explicitly time-dependent. The results from the quasiclassical formulation for a wide range of energies [1] were found to be in very good agreement with experimental results [6, 7] as well as theoretical ones available for higher excess energies [8, 9].

Moreover, our classical results allow for a detailed analysis of the physical processes in terms of the classical trajectories: As we have demonstrated, the triply photoionizing trajectories can be organized in groups according to the respective sequence of electron-electron collisions [10]. According to this collision scheme we have identified two main sequences that lead to triple ionization from the Li ground state. An indirect verification of the collision scheme could be achieved by measurement of

the electronic angular correlation probability: we have shown for excess energies close to threshold [10], that the classification scheme of ionizing trajectories can explain the electronic angular correlation probability in terms of the dominant “T-shaped” pattern of the three escaping electrons. The electronic angular correlation probability is not yet known experimentally. However, it should be measurable with state of the art experimental techniques.

In the current paper, we explore the manifestations in classical probability densities of the two main collision sequences the three electrons follow to ionize from the ground state of Li. While our previous treatment of the collision sequences was on the level of single trajectories [1, 10] we now treat them on the level of ensemble averages. Our motivation for doing so is that probability densities are the closest classical analog to quantum mechanics. In quantum mechanics the probability density is defined directly through the quantum mechanical wavefunction. In classical physics probability densities can be easily computed allowing for a visualization of the differences between classical and quantum mechanical observables and for exploring the correspondence principle. Our ideas should be a useful tool for identifying and understanding collision mechanisms in other systems where collision processes play an important role, e.g., strongly driven atomic systems.

Finally, the collision sequences in triple ionization of Li take place on an *attosecond* time scale. While the first collision, in each ionization path, occurs around a couple of attoseconds after photoabsorption the second collision takes place around 70 attoseconds. This is another interesting aspect of our work: the emergence of attosecond laser pulses represents one of the most exciting developments in ultrafast laser science over the past few years [11, 12]. Attosecond pulses raise the prospect of studying electronic wave-packet motion on the time scales at which this motion occurs in nature, namely, the atomic unit of time (1 a.u.=24 attoseconds). These time scales show why attosecond pulses are new tools for exploring electronic processes at their natural time-scale

and at dimensions shorter than even atomic-dimensions. The advancement of ultra-short laser science and its so far success in exploring and controlling electronic motion [13] renders a future direct experimental verification of our collision sequences possible.

## II. TIME-DEPENDENT QUASICLASSICAL DESCRIPTION OF IONIZATION

Typically, there are two structurally different contributions in quantum mechanical matrix elements  $\langle \psi_f | \mathcal{O}(t) | \psi_i \rangle$ , the wavefunctions  $\psi_{i,f}$  and the operator  $\mathcal{O}(t)$ . We call our description quasiclassical because we use the full wavefunctions  $\psi_i$  – exactly translated to a phase space density  $\rho(\gamma)$  through a Wigner transform – while the subsequent propagation of the density in time is performed fully classically. Here, we are interested in final states with all three electrons of Li in the continuum. Since we propagate the entire four body system over very long times, we can simply project onto momentum states (corresponding to a measurement at the detector). In practise, this is done by binning final momenta of trajectories, very similarly as in the experiment.

### A. The initial phase space density for single photon multiple ionization

The construction of the initial phase space density  $\rho(\gamma)$  in our quasiclassical formulation of the triple photoionization of Li has been detailed in [1], here we give only a brief summary. We formulate the triple photoionization process from the Li ground state ( $1s^2 2s$ ) as a two step process [9, 14, 15]. First, one electron absorbs the photon (photo-electron) at time  $t = t_{\text{abs}} = 0$ . Then, due to the electronic correlations, redistribution of the energy takes place resulting in three electrons escaping to the continuum. It is the latter step that we describe in our formulation. We first assume that the photo-electron is a  $1s$ -electron. It absorbs the photon at the nucleus ( $\mathbf{r}_1 = 0$ ), an approximation that becomes exact in the limit of high photon energy [16]. The photon could also be absorbed by the Li  $2s$ -electron. However, the cross section for photon absorption from a  $1s$  orbital is much larger than from a  $2s$  orbital [17]. Hence, we can safely assume that the photo-electron is a  $1s$  electron which significantly reduces the initial phase space to be sampled. Also, by virtue of their different character the electrons become practically distinguishable and allow us to neglect antisymmetrization of the initial state. We denote the photo-electron by 1, the other  $1s$  electron by 2 and the  $2s$  electron by 3. Immediately after photon absorption, we model the initial phase space distribution of the remaining two electrons,  $1s$  and  $2s$ , by the Wigner transform of the corresponding initial wavefunction  $\psi(\mathbf{r}_1 = 0, \mathbf{r}_2, \mathbf{r}_3)$ , where  $\mathbf{r}_i$  are the electron vectors starting at the nucleus. We approximate the initial wavefunction as a simple product of hydro-

genic orbitals  $\phi_i^{Z_i}(\mathbf{r}_i)$  with effective charges  $Z_i$ , to facilitate the Wigner transformation. The  $Z_i$  are chosen to reproduce the known ionization potentials  $I_i$ , namely for the  $2s$  electron  $Z_3 = 1.259$  ( $I_3 = 0.198$  a.u.) and for the  $1s$  electron  $Z_2 = 2.358$  ( $I_2 = 2.780$  a.u.). (We use atomic units throughout the paper if not stated otherwise.) The excess energy,  $E$ , is given by  $E = E_\omega - I$  with  $E_\omega$  the photon energy and  $I = 7.478$  a.u. the Li triple ionization threshold energy. Following these considerations, the initial phase space density is given by

$$\rho(\gamma) = \mathcal{N} \delta(\mathbf{r}_1) \delta(\varepsilon_1 + I_1 - \omega) \prod_{i=2,3} W_{\phi_i^{Z_i}}(\mathbf{r}_i, \mathbf{p}_i) \delta(\varepsilon_i + I_i) \quad (1)$$

with normalization constant  $\mathcal{N}$ .

To determine which fraction of  $\rho(\gamma)$  leads to triple ionization, the phase space distribution must be followed in time.

### B. The evolution of classical phase space densities

The evolution of a classical phase space density is determined by the classical Liouville equation, which may be obtained within the quantum mechanical phase space Wigner formalism [18] by taking the limit  $\hbar = 0$  [19, 20],

$$\frac{\partial \rho(\Gamma(t))}{\partial t} = \mathcal{L}_{\text{cl}} \rho(\Gamma(t)). \quad (2)$$

The initial phase space values are

$$\Gamma(0) \equiv \gamma, \quad (3)$$

and  $\mathcal{L}_{\text{cl}}$  is the classical Liouville operator which is defined by the Poisson bracket  $\{H, \}$ , with  $H$  the Hamiltonian of the system. In our case  $H$  is the full Coulomb four-body Hamiltonian. In practice, Eq. (2) amounts to discretizing the initial phase space, assigning weights to each discrete point  $\gamma_j = (p_j(0), q_j(0))$  according to  $\rho(\gamma_j)$ , and evolving in time each initial condition  $\gamma_j$  with the Coulomb four-body Hamiltonian. This amounts to propagating electron trajectories using the classical equations of motion (CTMC). Regularized coordinates [21] are used to avoid problems with electron trajectories starting at the nucleus.

### C. Different triple ionizing collision sequences and their phase space ensembles

An important finding of our previous studies [10] is that the triple ionizing trajectories can be organized in classes according to their ionization-driven properties. In particular, we found two main classes consisting of those trajectories that triply ionize through the (12,13) collision sequence and those that ionize through the (12,23) collision sequence. In the first class the path to ionization proceeds with photo electron 1 knocking out, successively, electrons 2 and 3. In the second class the photo-electron 1 first knocks out electron 2 and then, electron

2 knocks out electron 3. More abstractly speaking, each class defines an ensemble of trajectories which we label  $\alpha = \text{I}$  and  $\alpha = \text{II}$  for the (12,13) and the (12,23) collision sequences, respectively.

For completeness, we briefly describe what we define as a momentum transferring electron-electron collision along a trajectory with time dependent electron positions  $\mathbf{r}_i(t)$ ,  $i = 1, 2, 3$  (see [10]). The term responsible for momentum transfer between electrons  $i$  and  $j$  is their Coulomb repulsion  $V(r_{ij}) = r_{ij}^{-1}$ ,  $\mathbf{r}_{ij} = \mathbf{r}_i - \mathbf{r}_j$ . Hence, we identify a collision between electron  $i$  and  $j$  ( $ij$ ) through the momentum transfer

$$\mathbf{D}_{ij} := - \int_{t_1}^{t_2} \nabla V(r_{ij}) dt \equiv \int_{t_1}^{t_2} \mathbf{F}_{ij} dt \quad (4)$$

under the condition that  $V(r_{ij}(t_k))$ ,  $k = 1, 2$  are local minima in time with  $t_2 > t_1$ , while  $r_{ij} = |\mathbf{r}_i - \mathbf{r}_j|$ . This automatically ensures that the integral of Eq. (4) includes the “collision” with a local maximum of  $V(r_{ij}(t))$  at a time  $t_1 < t_M < t_2$ . During the time interval  $t_1 < t < t_2$ , all four particles interact with each other. Hence, the definition Eq. (4) is only meaningful if the collision redistributes energy dominantly within the subsystem given by the three-body  $\text{Li}^+$ -Hamiltonian,  $H_{ij}$ , of the nucleus and the electrons  $i$  and  $j$  involved in the actual collision,

$$H_{ij} = H_i + H_j + \frac{1}{|\mathbf{r}_i - \mathbf{r}_j|}, \quad (5)$$

with

$$\dot{H}_{ij} \equiv \frac{dH_{ij}}{dt} \approx 0 \text{ for } t_1 < t < t_2, \quad (6)$$

where

$$H_i = p_i^2/2 - Z/r_i \quad (7)$$

are hydrogenic two-body Hamiltonians with charge  $Z = 3$  of the Lithium ion.

Our goal is to investigate whether the two main ionization sequences we have previously identified using Eq. (4), manifest themselves on an ensemble average level with properties that clearly distinguish one from the other, thus reinforcing the validity of our classification scheme. To this end we need classical observables defined over arbitrary phase space ensembles  $\alpha$ , in our case the two ensembles I and II.

#### D. Classical probability densities for observables over a classical phase space ensemble

The probability density  $\mathcal{P}_\alpha(a, t)$  to find the value  $a$  for the observable  $A$  at time  $t$  under the ensemble  $\alpha$  is given by

$$\mathcal{P}_\alpha(a, t) = \int_\alpha \delta(a - A(\gamma, t)) \rho(\gamma) d\gamma, \quad (8)$$

where  $\int_\alpha d\gamma$  denotes integration over initial phase space which contains only those trajectories that belong to the ensemble  $\alpha$ . The propagation begins at the time  $t_{\text{abs}} = 0$  of photoabsorption. Eq. (8) amounts to a) propagating all the trajectories of the ensemble  $\alpha$  from time  $t_{\text{abs}}$  up to  $t$ , b) computing for each trajectory the observable  $A(t)$ , c) selecting only those trajectories which satisfy  $A(t) = a$  and adding together their weights. Note, that the probability to find at time  $t$  the value  $a$  for the observable  $A(t)$  is given by  $\mathcal{P}_\alpha(a, t) da$ .

Finally, the classical average of the observable  $A(t)$  over the ensemble  $\alpha$  is simply [22]

$$\langle A(t) \rangle_\alpha = \int_\alpha A(\gamma, t) \rho(\gamma) d\gamma. \quad (9)$$

### III. ENSEMBLE AVERAGES OF ENERGY AND THE MAIN COLLISION SEQUENCES

That the ensembles I and II, defined by the two main collision sequences, leave different traces on classical averages is obvious from Fig. 1. This and all other results have been obtained at an excess energy of  $E = 0.9 \text{ eV}$ , that is fairly close to threshold [1]. Firstly, we see in Fig. 1a that the electron pair potential energies  $\langle 1/r_{12} \rangle_{\text{I}}$  (solid line) and  $\langle 1/r_{13} \rangle_{\text{I}}$  (dashed line) have well defined maxima at  $t_{12} = 1.6$  and  $t_{13} = 65$  attoseconds, even when averaged over all trajectories that ionize through the (12, 13) collision sequence. Note that  $\langle 1/r_{23} \rangle_{\text{I}}$  (dotted line) decreases monotonically. Thus, all trajectories triply ionizing through the (12, 13) collision sequence, satisfy as an ensemble the first criterion of this sequence, namely, maxima in the potential energies of the electron pairs 12 and 13 participating in collisions. They also satisfy as an ensemble the second criterion, that is, while the  $\langle 1/r_{12} \rangle_{\text{I}}$  potential energy changes during the 12 collision the energy of the three-body Hamiltonian  $\langle H_{12} \rangle_{\text{I}}$ , see Eqs. 5, 6, remains constant and while the  $\langle 1/r_{13} \rangle_{\text{I}}$  potential energy changes during the 13 collision the energy of the three-body Hamiltonian  $\langle H_{13} \rangle_{\text{I}}$  remains constant. This is clearly demonstrated in Fig. 1b:  $\langle H_{12} \rangle_{\text{I}}$  (thin solid line) remains almost constant near  $t_{12} = 1.6$  as, while it changes around  $t_{13} = 65$  as, as should be the case since during the 13 collision it is the  $\langle H_{13} \rangle_{\text{I}}$  energy (thin dashed line) that is conserved. Similarly,  $\langle H_{13} \rangle_{\text{I}}$  remains constant around  $t_{13} = 65$  as, while it changes near  $t_{12} = 1.6$  as, since during the 12 collision it is the  $\langle H_{12} \rangle_{\text{I}}$  energy that is conserved. We also plot  $\langle H_{23} \rangle_{\text{I}}$  (thin dotted line) to demonstrate that it changes both, around the  $t_{12}$  and  $t_{13}$  collision times. One may summarize the two criteria for triple ionizing ensembles of trajectories as

- (A) A maximum in time of the ensemble average  $\langle 1/r_{ij} \rangle_\alpha$  defines a collision and its time  $t_{ij}$  between electrons  $i$  and  $j$ .
- (B) Near the time of collision  $t_{ij}$  the corresponding three-body energy  $\langle H_{ij} \rangle_\alpha$  of the ensemble remains approximately constant.

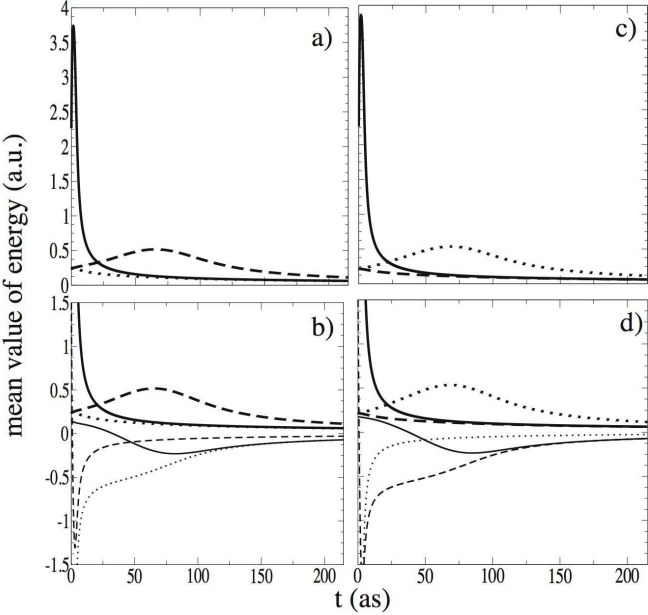


FIG. 1: Averages over ensembles  $\alpha = \text{I}$  (left, a–b)) and  $\alpha = \text{II}$  (right, c–d)), see Eq. (9). The upper panels show the interelectronic repulsions,  $\langle 1/r_{12} \rangle_\alpha$  (solid),  $\langle 1/r_{13} \rangle_\alpha$  (dashed), and  $\langle 1/r_{23} \rangle_\alpha$  (dotted). The lower panels show in addition the three-body energies with thin lines  $\langle H_{12} \rangle_\alpha$  (solid),  $\langle H_{13} \rangle_\alpha$  (dashed),  $\langle H_{23} \rangle_\alpha$  (dotted).

These criteria apply also to ensemble II for the collision sequence (12,23) as one can see in Figs. 1c and 1d. The collisions 12 and 23 are well defined and take place with maxima in  $\langle 1/r_{12} \rangle_{\text{II}}$  at  $t_{12} = 1.7$  as and in  $\langle 1/r_{23} \rangle_{\text{II}}$  at  $t_{23} = 69$  as, the corresponding three-body energies remain almost constant around these times.

It is important to keep in mind that the collisions described above are not binary but three-body collisions involving two electrons and the nucleus. If we were dealing with binary collisions then  $\langle p_i^2/2 + p_j^2/2 + 1/|\mathbf{r}_i - \mathbf{r}_j| \rangle$  instead of  $\langle H_{ij} \rangle$  would be constant during the  $ij$  collision, which is not the case as one can easily show. For simplicity we will identify in the following a collision by  $ij$ . However, it is always understood that the nucleus is part of the collision and that  $ij$  refers to the three-body Hamiltonian  $H_{ij}$  as given in Eq. (5).

#### IV. PROBABILITY DENSITIES

##### A. Position

The probability densities for the Cartesian positions of each of the three electrons  $i$ , given by Eq. (8) where  $A(\gamma, t) = q_i(\gamma, t)$  with  $q = x, y$  or  $z$ , do not offer much information regarding the identity of the electron pairs that participate in each collision, see Fig. 2. However, they contain information about the electron pairs during the collisions: Fig. 2 shows that the probability den-

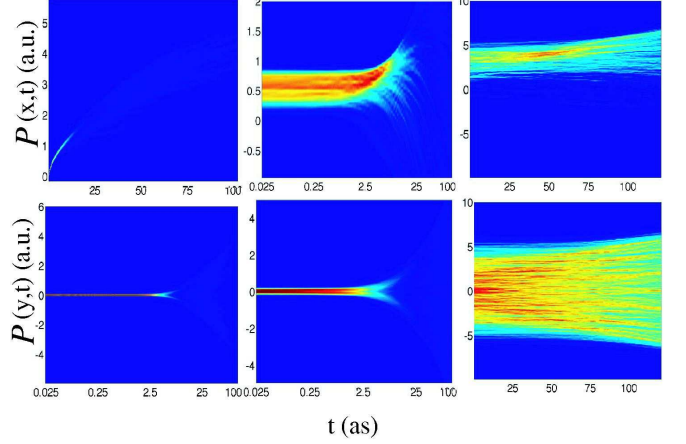


FIG. 2: Top panel:  $\mathcal{P}_\alpha(x_i, t)$  for electrons  $i = 1, 2, 3$  (from left to right) for the  $\alpha = \text{I}$  ensemble; Bottom panel: as for the top panel but for  $\mathcal{P}_\alpha(y_i, t)$ .

sity of the Cartesian coordinates of electrons 2 and 3 remain almost constant until 1.6 and 65 as, respectively, the times that electron 1 knocks them out in the 12 and 13 collisions of the (12,13) collision sequence. In addition, the probability density of the  $y$  and  $z$  component of the photoelectron 1 does not change up to 1.6 as, the time of collision of electron 1 with 2. This is expected for small times since the photoelectron's initial momentum is along the  $x$ -axis. Similar conclusions can be drawn for the (12,23) collision sequence.

Due to our choice of initial conditions for the photoelectron (electron 1 always starts at  $\mathbf{r} = 0$  with initial momentum along the  $x$ -axis) our model has cylindrical symmetry around the  $x$ -axis. As a result the probability density of  $y_i$  is equal to that of  $z_i$ . Moreover, since the invariance under the parity operation  $y \rightarrow -y$  of the Hamiltonian is not broken through the initial conditions, Eq. (1), the corresponding distributions  $\mathcal{P}(y_i, t)$  are symmetric about  $y_i = 0$ , the same holds of course for the  $z_i$ -coordinates and for all times, see Fig. 2. These symmetry properties extend to observables which respect them, such as, e.g., individual electron momenta.

##### B. Momentum

The probability densities of the Cartesian momentum components for each of the electrons allow for a deeper insight into the mechanism of the electron collisions taking place during the two main sequences. During an  $ij$  collision the transfer of energy between electrons  $i$  and  $j$  is mediated through their mutual repulsion,  $V(r_{ij})$ . As discussed above, we have defined the collision time  $t_{ij}$  as the time  $\dot{V}(r_{ij}) = 0$  with  $V_{ij}$  maximal, see Eq. (4). However, a collision may formally be defined to last between two minima of  $V_{ij}$  at times  $t_1 < t_{ij}$  and  $t_2 > t_{ij}$ . During the time the two electrons approach each other,  $t_1 < t < t_{ij}$ ,

$\dot{V}(r_{ij}) > 0$ , while for  $t_{ij} < t < t_2$ ,  $\dot{V}(r_{ij}) < 0$ .

This has different consequences for the corresponding time evolutions of the individual hydrogenic energies  $H_i(t)$  of the two electrons, Eq. (7), the one which suffers a net loss of energy in the collision (the impacting electron) and the one which overall gains energy in the collision (the impacted electron), see Fig. 3. The latter gains energy throughout the collision that is,  $\dot{H}_j > 0$  for  $t_1 < t < t_2$ . On the other hand, the impacting electron loses energy up to a time  $t_s$ , that is  $\dot{H}_i < 0$  for  $t_1 < t < t_s$  with  $t_s > t_{ij}$  ( $t_s > t_{ij}$  follows from Eqs. (5, 6) and  $\dot{V}(r_{ij}) = 0$  at time  $t_{ij}$ ) while for  $t_s < t < t_2$  the impacting electron gains energy  $\dot{H}_i > 0$ . From Eqs. (5) and (6) we can determine the change of a hydrogenic energy  $H_j$  in time during a collision with electron  $i$ . On the one hand we have

$$\frac{dH_j}{dt} = \mathbf{p}_j \cdot \dot{\mathbf{p}}_j + \frac{\partial H_j}{\partial \mathbf{r}_j} \cdot \mathbf{p}_j. \quad (10)$$

On the other hand we have

$$\dot{\mathbf{p}}_j \approx -\frac{\partial H_{ij}}{\partial \mathbf{r}_j} = \mathbf{F}_{ij} - \frac{\partial H_j}{\partial \mathbf{r}_j}. \quad (11)$$

Inserting Eq. (11) into Eq. (10) leads to

$$\frac{dH_j}{dt} = \mathbf{p}_j \cdot \mathbf{F}_{ij}, \quad (12)$$

which shows, that the change of the hydrogenic energy of electron  $j$  does not only depend on the modulus of the electron-electron force  $\mathbf{F}_{ij}$  but also on its direction relative to the momentum  $\mathbf{p}_j$  of electron  $j$ . We recall at this point that the present analysis of the collision sequences in terms of the rate of change of the single electron energies  $H_i$  does by no means imply that we have calculated the evolution of trajectories with  $H_i$ . All observables are evaluated with our numerical results for the triple ionizing trajectories from the propagated full four-body Coulomb Hamiltonian, as we have already pointed out in section II A.

In Fig. 3 the ensemble averages  $\langle H_i \rangle_\alpha$  clearly illustrate the difference between the impacting and the impacted electron for each three-body collision. For trajectories from the ensemble  $\alpha = I$  (Fig. 3a) electron 1 transfers energy to electron 2 during the 12 collision as can be seen from the sharp decrease of  $\langle H_1 \rangle_I$  followed by an increase beginning at  $t = 2.4$  as while at the same time the energy  $\langle H_2 \rangle_I$  of the impacted electron 2 increases. The pattern is repeated during the 13 collision where a decrease in  $\langle H_1 \rangle_I$  is followed by an increase at 79 as, while at the same time  $\langle H_3 \rangle_I$  of the impacted electron 3 is increasing. The pattern of the hydrogenic energies during collisions is also fulfilled for the ensemble II as can be seen in Fig. 3b.

Describing the collisions using the rate of change of the single electron Hamiltonians has the advantage that the effect of the nucleus is “folded in”. As a result both, the early collision which takes place close to the nucleus and

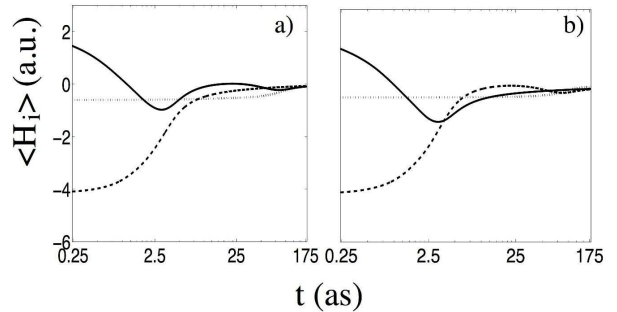


FIG. 3: Single electron energy averages  $\langle H_i \rangle_\alpha$  of electrons 1 (solid), 2 (dashed), 3 (dotted) for the ensemble  $\alpha = I$  (a) and  $\alpha = II$  (b).

the latter one which takes place far away from it (for both ensembles I and II), exhibit exactly the same pattern, see Fig. 3. This becomes even clearer when one compares Fig. 3 with the probability densities of the momentum component along the  $x$ -direction for all three electrons in Figs. 4, 5 and 6. The momentum along the  $x$ -direction of the impacting electron 1 in ensemble I switches from decreasing to increasing at times 3.5 as for the 12 collision and 79 as for the 13 collision. This is a consequence of  $H_1$  switching sign at 2.4 as for the 12 and at 79 as for the 13 collision. The time of 3.5 as, where  $p_{x,1}$  starts to increase in the 12 collision, is different from the time 2.4 as, where  $\dot{H}_1$  switches sign, while both times are the same in the 13 collision. The reason is that for the 12 collision the  $x, y, z$ -coordinates are not equivalent, with the transfer of momentum taking place mainly along the  $x$ -direction, while for the later 13 collision the  $x, y, z$ -coordinates are almost equivalent. This is illustrated in Fig. 7, with  $\mathbf{p}_1 \cdot \mathbf{F}_{21} = 0$  at 2.4 as and  $\mathbf{p}_{x,1} \cdot \mathbf{F}_{21} = 0$  at 3.5 as. The nucleus has a significant effect on the 12 collision while it has a small one on the 13 collision as seen by the more prominent increase of  $p_{x,1}$  at 79 as when compared to its increase at 3.5 as. The change with time of  $p_{x,1}$  during the 12 collision is due to  $\mathbf{F}_{21}$  and the  $-\partial H_1 / \partial \mathbf{r}_1$  force from the nucleus, while in the 13 collision the change of  $p_{x,1}$  is mainly due to  $\mathbf{F}_{31}$ . In Figs. 5 and 6 we see that  $p_{x,2}$  and  $p_{x,3}$  increase during the time the respective electrons 2 and 3 are impacted by electron 1, in agreement with  $\dot{H}_2 > 0$  and  $\dot{H}_3 > 0$  during the 12 and 13 collisions. Similar conclusions can be drawn for the  $\alpha = II$  ensemble.

### C. Inter-electronic angles

Finally, we discuss the time evolution of the inter-electronic angles. For large times and quasi-free motion  $\mathbf{r}_i \propto \mathbf{p}_i t$ , the inter-electronic angles refer to the relation between positions as well as momenta of the electrons. The dynamics in the angle is governed by two principles:

- (A) Collisions between two electrons lead to a minimum of the angle  $\theta_{ij}$  between the participating electrons

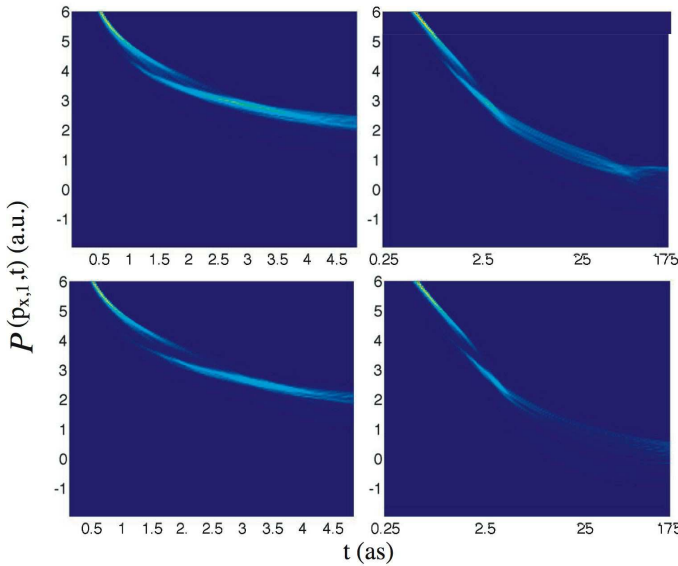


FIG. 4: Momentum distributions  $\mathcal{P}_\alpha(p_x, t)$  for electron 1 for the  $\alpha = \text{I}$  (top) and  $\alpha = \text{II}$  (bottom) ensemble. The left panels show the evolution for short times in greater detail.

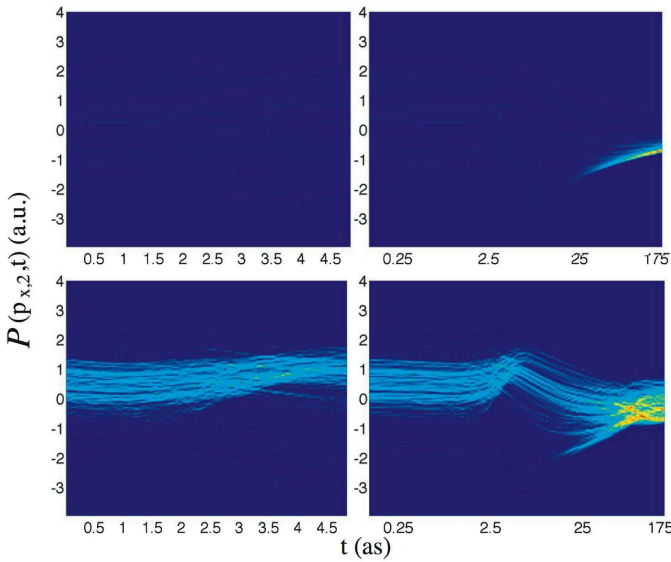


FIG. 5: Same as Fig. 4 but for electron 2.

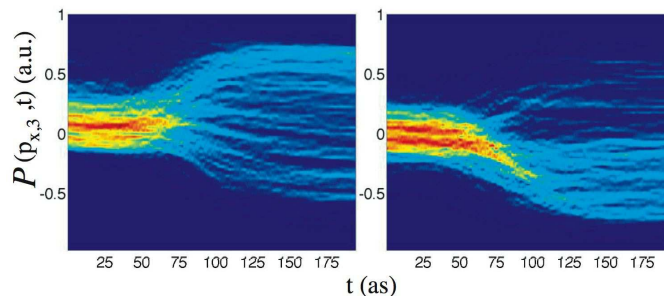


FIG. 6: Momentum distribution  $\mathcal{P}_\alpha(p_x, t)$  for electron 3 for the  $\alpha = \text{I}$  (left) and  $\alpha = \text{II}$  (right) ensemble.

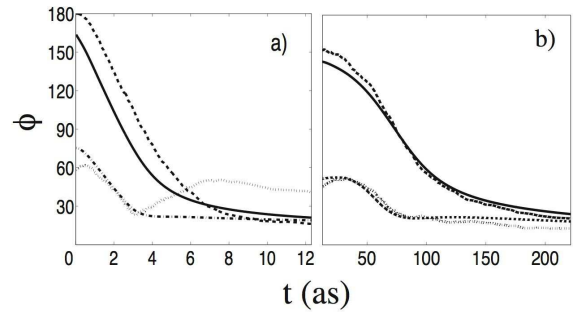


FIG. 7: Averaged angles as a function of time over the  $\alpha = \text{I}$  ensemble. Solid: angle  $\phi$  between  $\mathbf{F}_{21}$  and  $\mathbf{p}_1$  in a) and between  $\mathbf{F}_{31}$  and  $\mathbf{p}_1$  in b); Dashed: angle  $\phi$  between  $\mathbf{F}_{21}$  and  $\mathbf{p}_{x,1}$  in a) and between  $\mathbf{F}_{31}$  and  $\mathbf{p}_{x,1}$  in b); Dash-dotted: angle  $\phi$  between  $\mathbf{F}_{12}$  and  $\mathbf{p}_2$  in a) and between  $\mathbf{F}_{13}$  and  $\mathbf{p}_3$  in b); Dotted: angle  $\phi$  between  $\mathbf{F}_{12}$  and  $\mathbf{p}_{x,2}$  and between  $\mathbf{F}_{13}$  and  $\mathbf{p}_{x,3}$  in b).

$i$  and  $j$ , i.e.,  $\theta_{ij}(t_{ij}) \approx 0$ , if the collision happens at time  $t_{ij}$ .

(B) Electrons tend to move away from each other minimizing their mutual repulsive interaction. This leads to an interelectronic angle of  $180^\circ$ , if none of the electrons suffers a collision through the third electron.

With these two principles, we recognize in Fig. 8 the first collision early on (small angle, criterion A) and we also infer that a second collision happens around 65 as, but *not* between electrons 1 and 2, since suddenly the increase of their mutual angle towards  $180^\circ$  (criterion B) is stopped and  $\theta_{12}$  shrinks again towards its final value of  $90^\circ$ , giving rise to the “T-shape” structure of the three escaping electrons [10]. This is true for both collision sequences, (12,13) and (12,23). The first collision happens in both cases between electrons 1 and 2, and then electron 3 imposes a second collision with one of the partners forming the angle in Fig. 8, namely with electron 1 (upper panels) and electron 2 (lower panels). Finally, since in both cases the last colliding electron pair is not the 12,  $\theta_{12}$  approaches  $90^\circ$ .

The evolution of  $\mathcal{P}(\theta_{13})$ , Fig. 9, and  $\mathcal{P}(\theta_{23})$ , Fig. 10, differs much more for the respective two sequences (upper and lower panels). However, there is a similarity across the two figures, namely the pattern in the upper(lower) panel of Fig. 9 is similar to that in the lower(upper) panel of Fig. 10.

The reason is that in the case of  $\theta_{13}$  only the  $\alpha = \text{I}$  ensemble (upper panel of Fig. 9) leaves the visible imprint of a collision, bringing  $\theta_{13}$  close to zero while it rapidly approaches  $180^\circ$  afterwards, since it is the last collision and electrons 1 and 3 move away from each other afterwards. The same, but now for electrons 2 and 3, is true for the  $\alpha = \text{II}$  ensemble (lower panel of Fig. 10).

In the other two panels (lower panel of Fig. 9 and upper panel of Fig. 10) one recognizes with the sudden turn

away from  $180^\circ$  for the respective interelectronic angle a collision with the third electron (criterion B), in case of Fig. 9 the collision partner is electron 2 and in case of Fig. 10 electron 1.

Finally, it is worthwhile to note and understand the great variation in the width of the initial distribution for the angles across the three figures.  $\mathcal{P}(\theta_{12}, 0)$  is most strongly confined to values around zero since the 12-collision happens at an early time and electron 1, having absorbed the photon energy, starts with relatively high velocity close to the origin (position of the nucleus). In the short time (1.7 as) before the collision the momentum vector of electron 1 cannot change substantially, so electron 1 keeps its direction.

The condition for the first collision,  $r_1(t_{12}) \approx r_2(t_{12})$ , implies also that the angles  $\theta_{13}$  and  $\theta_{23}$  should be similar at early times. This is indeed the case, comparing the upper left panels of Figs. 9 and 10, where in both cases the maximum of the initial distribution is around  $50^\circ$ , while for the lower left panels the widely spread initial distribution is centered about  $90^\circ$ . The latter indicates no clear preference in the initial mutual angle between electrons 2 and 3 reflecting the expectation value of an uncorrelated (product) wavefunction for the Lithium ground state as used here. Moreover, one should keep in mind that whenever electron 3 is involved one would expect a wider distribution due to the larger size of the  $2s$  initial electron density compared to the  $1s$  density for electrons 1 and 2.

## V. CONCLUSIONS

We have investigated the two main collision paths the three electrons follow to escape to the continuum from the ground state of Li after single photon absorption on an ensemble level. Studying the classical probability densities for the two ensembles of trajectories corresponding to the two main collision sequences we were able to identify the traces these sequences leave on the classical probability densities. Furthermore, we could show that each of the two ensembles has unique manifestations on the ensemble average level which clearly distinguish one from the other. Being able to distinguish the two main attosecond time scale collision sequences on an ensemble level holds promise for a future *direct* observation of these collision sequences with the advancement of ultra-short laser technology.

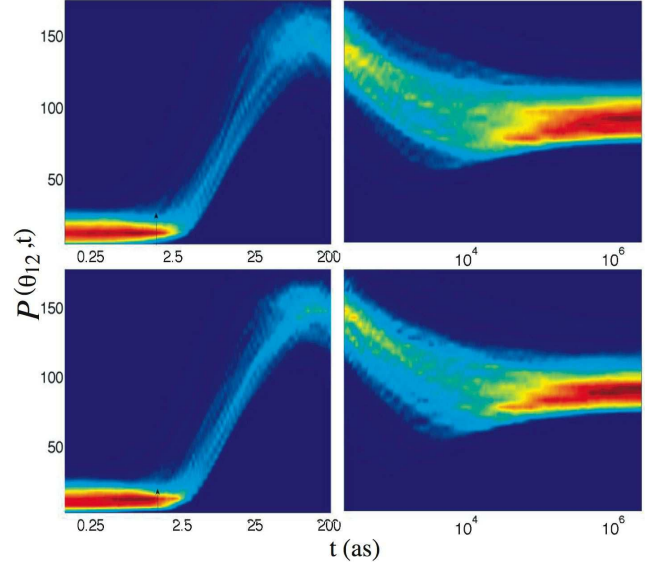


FIG. 8: Same as Fig. 4 but for the probability density of the inter-electronic angle  $\theta_{12}$ ,  $\mathcal{P}_\alpha(\theta_{12}, t)$ . The arrows indicate the time of the collision  $t_{ij}$ .

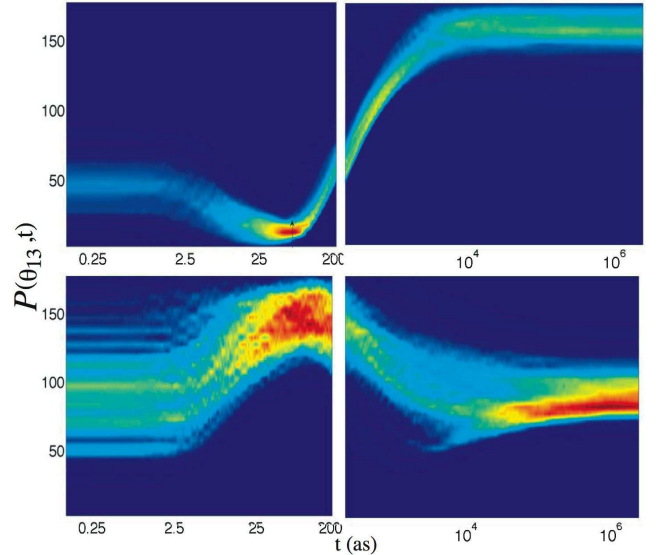


FIG. 9: Same as in Fig. 8 but for the inter-electronic angle  $\theta_{13}$ .

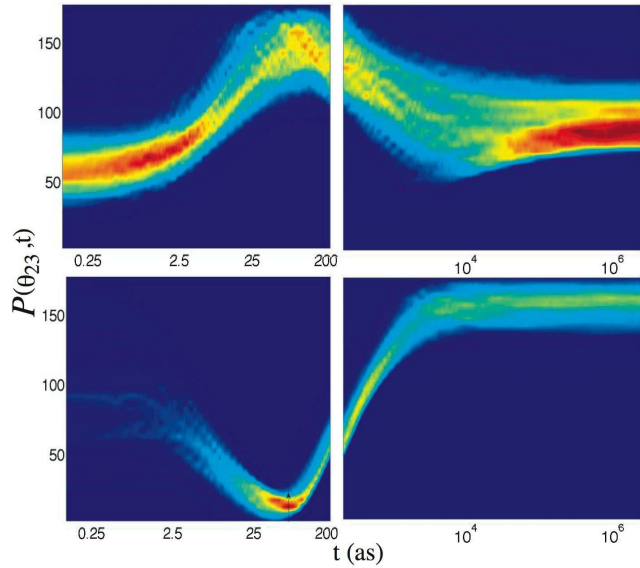


FIG. 10: Same as in Fig. 8 but for the inter-electronic angle  $\theta_{23}$ .

---

[1] A. Emmanouilidou and J.M. Rost, *J. Phys. B* **39**, L99 (2006).

[2] R. Abrines and I.C. Percival *Proc. Phys. Soc. London* **88**, 861 (1966).

[3] D.J.W Hardie and R.E. Olson *J. Phys. B: At. Mol. Phys.* **16** 1983 (1983).

[4] D. Eichenauer, N. Grün and W. Scheid, *J. Phys. B: At. Mol. Phys.* **14**, 3929 (1981).

[5] J.S. Cohen *J. Phys. B: At. Mol. Phys.* **18**, 1759 (1981).

[6] R. Wehlitz, M-T Huang, B.D. DePaola, J.C. Levin, I.A. Sellin, T. Nagata, J.W. Cooper and Y. Azuma, *Phys. Rev. Lett.* **81**, 1813 (1998).

[7] R. Wehlitz, T. Pattard, M-T Huang, I.A. Sellin, J. Burgdörfer and Y. Azuma, *Phys. Rev. A* **61**, 030704 (2000).

[8] J. Colgan, M. S. Pindzola, and F. Robicheaux, *Phys. Rev. Lett.* **93**, 053201 (2004); *Phys. Rev. A* **72**, 022727 (2005).

[9] T. Pattard and J. Burgdörfer, *Phys. Rev. A* **63**, 020701(R) (2001).

[10] A. Emmanouilidou and J.M. Rost, *J. Phys. B* **39**, 4037 (2006).

[11] P. Agostini and L. F. DiMauro, *Rep. Prog. Phys.* **67**, 813 (2004).

[12] M. Yu. Ivanov and I. A. Walmsley, *J. Mod. Opt.* **52**, No. 2-3 (2005).

[13] M. Drescher, M. Hentschel, R. Kienberger, M. Uiberacher, V. Yakovlev, A. Scrinziand, th. Westerwalbesloh, U. Kleineberg, U. Heinzmann and F. Krausz, *Nature* **419**, 803 (2002).

[14] T. Schneider, P. L. Chocian, and J. M. Rost, *Phys. Rev. Lett.* **89**, 073002 (2002).

[15] J. A. R. Samson, *Phys. Rev. Lett.* **65**, 2861 (1990).

[16] P. K. Kabir and E. E. Salpeter, *Phys. Rev.* **108**, 1256 (1957).

[17] A. Emmanouilidou, T. Schneider and J. M. Rost, *J. Phys. B* **36**, 2714 (2003).

[18] E. Wigner *Phys. Rev.* **40**, 749 (1932).

[19] E.J. Heller, *J. Chem. Phys.* **65**, 1289 (1976).

[20] T. Geyer and J. M. Rost *J. Phys. B* **35**, 1479 (2002).

[21] P. Kustaanheimo and E. Stiefel, *J. Reine Angew. Math.* **218**, 204 (1965).

[22] J.M. Rost, *Phys. Rep.* **297**, 271 (1998).